Biological tissue imaging with time-of-flight secondary ion mass spectrometry and cluster ion sources

Alain Brunelle, David Touboul, Olivier Laprévote

▶ **To cite this version:**

Alain Brunelle, David Touboul, Olivier Laprévote. Biological tissue imaging with time-of-flight secondary ion mass spectrometry and cluster ion sources. Journal of Mass Spectrometry, 2005, 40 (8), pp.985-999. 10.1002/jms.902 . hal-03976550

HAL Id: hal-03976550
https://hal.science/hal-03976550v1

Submitted on 13 Feb 2023

HAL is a multi-disciplinary open access archive for the deposit and dissemination of scientific research documents, whether they are published or not. The documents may come from teaching and research institutions in France or abroad, or from public or private research centers.

L'archive ouverte pluridisciplinaire **HAL**, est destinée au dépôt et à la diffusion de documents scientifiques de niveau recherche, publiés ou non, émanant des établissements d'enseignement et de recherche français ou étrangers, des laboratoires publics ou privés.

SPECIAL FEATURE: TUTORIAL

Biological Tissue Imaging with Time-of-Flight Secondary Ion Mass Spectrometry and Cluster Ion Sources

Alain Brunelle,* David Touboul & Olivier Laprévote

Laboratoire de Spectrométrie de Masse, Institut de Chimie des Substances Naturelles, CNRS, UPR 2301, Av. de la Terrasse, F91198, Gif-sur-Yvette Cedex, France

* Correspondence should be addressed to:

Alain Brunelle

Laboratoire de Spectrométrie de Masse, Institut de Chimie des Substances Naturelles

CNRS, Avenue de la Terrasse, F-91198 Gif sur Yvette Cedex

Tel: 33 (0) 169 824 575

Fax: 33 (0) 169 077 247

Alain.Brunelle@icsn.cnrs-gif.fr

Abstract

Time-of-flight secondary ion mass spectrometry (TOF-SIMS) using liquid metal ion guns (LMIGs) is now sensitive enough to produce molecular ion images directly from biological tissue samples. Primary cluster ions strike a spot on the sample to produce a mass spectrum. An image of this sample is achieved by rastering the irradiated point over the sample surface. The use of secondary ion mass spectrometry for mapping biological tissue surfaces provides unique analytical capabilities; in particular, it enables in a single acquisition a large variety of biological compounds to be localized on a micrometer scale and scrutinized for co-localisations. Without any treatment of the sample, this method is fully compatible with subsequent and complementary analyses like fluorescence microscopy, histochemical staining, or even matrix-assisted laser desorption/ionisation imaging. Basic physical concepts, required instrumentation (ion source and mass analyzer), sample preparation methods, image acquisition, image processing, and emerging biological applications will be described and discussed.

Keywords:

tutorial; mass spectrometry; imaging; biological tissue; time-of-flight; secondary ion mass spectrometry; cluster ion source

Introduction

Among the different techniques that allow mapping the surface of a biological tissue, mass spectrometry imaging makes it possible to access to the spatial distribution of several chemical compounds in only one scan. Contrary to affinity-based methods like immunochemistry or fluorescence microscopy for which specific molecules need to be preliminarily targeted, biological tissue imaging using mass spectrometry is not limited to *a priori* known molecules. Important applications, such as diagnostic imaging for several genetic and neurodegenerative diseases, are beginning to be found in the field of human health. Today two different and complementary techniques coexist. Ion microprobes based on secondary ion mass spectrometry were initially developed in the 60s.[1] Benninghoven was the first to use this technique to localize molecular ions on a surface.[2] The mass resolution and the transmission efficiency of SIMS were subsequently improved by Chait and Standing who used a time-of-flight analyzer to measure the masses of the biological compounds.[3] During the last years of the 20th century, Caprioli and co-workers[4,5] made an important breakthrough in the field of mass spectrometry imaging by taking advantage of the capabilities of matrix-assisted laser desorption/ionisation (MALDI). This method is known to produce intact ions from large biomolecules, like peptides and proteins, with molecular weights of thousands of Daltons.[6] In such MALDI imaging experiments, the lateral resolution is usually limited to the laser spot size, which is about ~25-50 μm. The matrix is deposited onto the biological tissue sample by devices like air sprays, and the homogeneity of its deposition remains always one of the most critical steps in sample preparation. Although the upper limit of the mass range in MALDI-MS images may possibly extend to several thousands of Daltons, it is by contrast difficult to record images of ions

having a mass to charge ratio in the same range to that of matrix ions, *i.e.* below *m/z*~500. This drawback has been partially worked around by the use of a tandem mass spectrometer, but in that particular case, the lateral resolution was limited to several hundreds of microns.[7] The TOF-SIMS technique, which by comparison is limited to ions like the phosphatidylcholine head-group at *m/z* 184,[8] can achieve a lateral resolution approaching a few tens of nanometers by using focused ion beams. Historically, the ion sources commonly used in TOF-SIMS experiments have been Ga^+ or In^+ liquid metal ions guns (LMIGs);[9] these provide excellent lateral resolutions but poor desorption efficiencies. Two recent reviews show the state of the art using TOF-SIMS instruments in biological sciences and in many other fields.[10,11]

Several methods to enhance the desorption efficiency of SIMS and to extend the mass range towards higher masses are currently being explored. Motivated by improvements obtained in spectroscopy experiments, several groups have tried to coat the biological tissue surface with different kinds of compounds, like silver, in order to produce secondary ions cationized by silver ions,[12] or even a MALDI matrix deposited by an electrospray device.[13] It has been shown that these methods increase the production of some secondary ions like cholesterol. Nevertheless, the interpretation of the spectra is made more difficult because of the presence of matrix ion peaks, which can interfere with ion peaks from the sample itself. Furthermore, the lateral resolution is limited to the size of the matrix crystals, which is generally of the order of several micrometers; hence, the matrix deposition procedure is of primary importance.

A second way that has recently been investigated to upgrade the performances of TOF-SIMS imaging has been to take advantage of the extraordinarily efficient gold and bismuth cluster ion sources. Gold cluster LMIGs have been in use for several years,[14]

but early attempts to fit this kind of ion source onto TOF-SIMS mass spectrometers were met with technical difficulties, like the need for primary ion selection. When employed for the first time in biological ion imaging, liquid ion sources, which deliver beams of cluster-ions like Au_3^+, Bi_3^+ or Bi_5^{2+}, produced significantly enhanced images. Now it is possible to routinely obtain secondary ion images with a mass range extended to more than 700 Daltons without any treatment of the sample and with a sub-micron lateral resolution.[15,16]

In this paper, we discuss a new method for mapping biological compounds at the tissue level that is aided by what can now be called "Cluster-TOF-SIMS-Imaging". In this microprobe approach, a focused ion beam irradiates a single, defined spot on the sample. The resulting mass spectrum is stored along with the spatial coordinates of the spot. A new adjacent pixel is then irradiated and another mass spectrum recorded. The process is repeated until the entire area has been mapped. The ion images are reconstructed from the individual mass spectra after the end of the experiment. The spatial resolution is of the order of one micrometer, or less, and the field of view can reach several square centimetres. Further, as the method does not destroy the sample, it is fully compatible with subsequent and complementary analyses like fluorescence microscopy, histochemical staining, or even MALDI-MS imaging. Although the instruments and the technology are well optimized and robust, the application of the method to animal or human tissue imaging is currently at a very early stage and only examples from a few diseases have been examined. Another method which is called the microscope mode[17] is also available but will not be described in the present paper. In this method secondary ions produced the primary ion shots pass through the time-of-

flight mass spectrometer forming an ion-optical image on a position-sensitive detector, as in wide-field optical microscopy.

Physical Background of Secondary Ion Emission under Ion and Cluster Impacts

Secondary Ion Mass spectrometry is based upon the emission of ions after the impact of energetic primary ions on the surface of a sample. A detailed description of the collision cascade theory, relatively to SIMS, has been recently written by Urbassek.[18] When an ion impinges on the surface of a solid, it penetrates the bulk up to a certain depth, depositing energy along its track. The way this energy is deposited depends mainly on the velocity of the primary ion. In the energy range of the present paper, a few keV to a few tens of keV, the energy is deposited through nuclear collisions. The energy loss per unit length is then called the nuclear stopping power - in comparison with the electronic stopping power, which is the energy lost by a projectile through interactions with the electron cloud in the solid and which dominates at much higher velocity, above ~0.2 cm.nsec^{-1}, *i.e.* at MeV energies for atomic ions. This deposited energy produces collision cascades and sets atoms of the bulk into motion. As the energy deposited is much higher than binding energies, it leads to intense fragmentations and bond breaking near the projectile track, producing mainly the emission of atomic particles. Moving laterally away from the projectile track, the density of energy deposited decreases, producing fewer and fewer fragmentations. Some intact molecules can then be emitted from the first layers near the surface if they acquire enough energy to overcome the surface binding energy. Among them, the majority are emitted as neutrals (~99.9% or more) and only a very small fraction are positively or negatively charged.

If the collision cascades are linear, which means that a moving atom hits mainly atoms which are at rest, the sputtering yields are well described by the theory developed in 1969 by Peter Sigmund.[19] In this model the sputtering yields are proportional to the

energy loss per unit length at the surface, divided by the surface binding energy. The nuclear stopping power increases with increasing velocity up to a maximum depending on the projectile-target combination. It also increases with the mass of both the projectile and the target and can be tabulated with the well known SRIM (Stopping and Ranges of Ions in Matter) code.[20] When the energy density becomes too high, experimental sputtering yields deviate from this linear cascade theory. Non-linear collision cascades are then generated, in which moving atoms may collide with atoms that are already in motion. Other models must be applied to explain the high sputtering yields. The most commonly used is the thermal spike model of Sigmund and Claussen;[21] however, other models like those described by a shockwave expansion[22] also exist. In the thermal spike model, the sputtering yield is proportional to the square of the nuclear energy loss. The transition from sputtering to secondary ion emission is generally not obvious, and no predictive model exists at all. Nevertheless, it is generally observed that in the energy range of a few keV to a few tens of keV the molecular ion emission is to the first order proportional to the square of the nuclear stopping power.[23]

A simple way to increase the energy density deposited close to the surface is to replace the atomic projectiles with polyatomic ones. This expedient offers the unique possibility of simultaneously bombarding a very small area with several atoms. The overlaps between the cascades started by individual atoms can give rise to various effects, like crater formation, material modifications, and secondary emission yields (ions, neutrals) that are much larger than would be induced by the same number of constituents arriving individually. Usually called nonlinear, these effects were first observed 30 years ago in sputtering of neutral species by Andersen and Bay.[24,25] Appelhans and Delmore then compared the secondary ion emission induced by SF_6^- and by Cs^+ ions,[26] and later

Benguerba *et al* used keV energy Au_n^+ (n = 1-5) gold clusters produced by a LMIG to study secondary ion emission of different organic and inorganic compounds.[14] A strong increase of the secondary ion emission was observed when switching from gold ions to gold clusters (Figure 1). Although it does not account for the ionisation efficiency, molecular dynamic simulations can give a good overview of the phenomena created by cluster impacts. Particularly, those performed by Colla *et al* showed the formation of large craters surrounded by a rim, from which large size species mainly come.[27] In addition they showed that fluctuations of the crater size and of the sputtering yields, which occur for atomic projectiles, decrease with increasing the number of constituents in the projectile.

Another important feature of the polyatomic projectiles concerns the relationship between the depth in the solid to which the incident energy is deposited, and the depth from which secondary ion emission can occur. Although it is generally admitted that SIMS belongs to the surface analysis techniques, one should be careful about what is called a surface. From measurements on stacks of different Langmuir-Blodgett monolayers, it has been found that more than 90% of the secondary ion emission comes from a depth of ~10 nm.[28] A cluster having several constituents has a lower energy per constituent and a lower velocity than an atomic projectile having the same total energy. Therefore, this cluster deposits a larger amount of its energy in the first layers of the solid, just below the surface where the secondary ion emission occurs. This explains the secondary ion emission increases when clusters replace atomic projectiles and why, at the same incident energy, C_{60}^+ projectiles can produce a higher secondary ion emission yield than Au_3^+ or Au_4^+ particles.[29]

Instrumentation

Time-of-flight analysers, Post acceleration, Detector, Time-to-Digital-Converter, Flood gun, Mass Calibration

Although the present paper only deals with TOF-SIMS, it must be noted that usage of TOF analyzers has become widespread due to their high transmission, parallel detection of all masses, and in principle, unlimited mass range. Since the advent of MALDI some 15 years ago, the TOF analyzers have become much more popular than before and most of the recent static SIMS mass spectrometers are built with a TOF analyzer.

A TOF analyzer separates secondary ions according to their mass to charge ratio *m/z*. All the secondary ions produced after the impact of a primary ion pulse are accelerated to the same kinetic energy *E* and then allowed to fly through a field free region of length *L*. The ion time-of-flight values *t* are related to mass by the equation: $t = L\sqrt{\frac{m}{2zE}}$. The primary ions need to be accelerated in pulses with durations equal to or shorter than one nanosecond. The final mass resolving power $M/\Delta M$ is equal to half of the time resolving power $t/\Delta t$ and depends on both the mass resolution of the analyzer and the duration of the primary ion pulse.

Complete descriptions of time-of-flight analysers and of the ion dynamics in these analyzers can be found in tutorials by Guilhaus[30] and Uphoff *et al*.[31] and in the book by Cotter.[32,33.] In essence, a linear TOF analyzer is little more than a field free tube inserted between an ion source from which the secondary ions are extracted and a detector with which they are recorded. Such basic analyzers are never quite used in SIMS because the mass resolution cannot be made larger than ~1000-1500 with a field free path of ~1 m. This limitation is due to the initial kinetic energy spread and angular distribution of the

secondary ions and is the reason why most of the TOF analyzers of SIMS instruments are fitted with an electrostatic mirror. This essential device, originally introduced by Mamyrin and co-workers,[34,35] elongates the field free path *L* and, more importantly, compensates for the differences in time of flight between ions of same *m/z* but a distribution in the kinetic energy as mentioned above. The resulting mass resolution $M/\Delta M$ is frequently ~15 000.

After separation by the TOF analyzer, the ions need to be detected with the highest efficiency. In TOF-SIMS instruments the ions fly with a kinetic energy of only a few keV, which does not ensure sufficient velocity for these ions to be efficiently detected. The detector needs consequently to be preceded by a post-acceleration stage that pushes the ions to a kinetic energy in the range of 10 to 20 keV, which is enough to maximize the detection efficiency below *m/z* 1000-1500.[36] The detectors can either be a dual chevron microchannel plate or a hybrid system made of one single microchannel plate followed by a scintillator and a photomultiplier.[36] The latter has several advantages, the most significant being a wider dynamic range. The electronic pulses coming from the detector are triggered by a constant fraction discriminator before feeding a time to digital converter.

Due to the very low initial kinetic energy distribution of the secondary ions in SIMS (compared to MALDI) and because of the very high precision of time to digital converters (these devices have a very good linearity over the full range and can have time bins as narrow as 50 ps), the relationship between $(m/z)^{½}$ and the time of flight remains linear over the whole mass range. Internal mass calibration can consequently be based on light mass fragment ions that are always present in the spectra, for example H^+, C^+, CH^+, CH_2^+, and $C_3H_2^+$ ion peaks in the positive ion mode and H^-, C^-, CH^-, CH_2^-,

C_2^-, C_3^-, C_4^-, and C_4H^- ion peaks in the negative ion mode. Then, this mass calibration can be refined step by step using identified ions of larger *m/z*. The deduced mass accuracies are in the vicinity of a few ppm.[37] The mass assignments are strengthened by the isotopic distribution, by the parity of the *m/z* value indicating the number of nitrogen atoms, and by a careful scrutiny of the mass spectra, mass differences between groups of peaks, etc...

If the irradiated sample surface is not conductive, the arrival of the primary ions, plus the extraction of the secondary ions, whatever their polarity, may rapidly cause the production of a surface charging that strongly disturbs the secondary ion time-of-flight and even the secondary ion emission. For that reason, TOF-SIMS mass spectrometers take benefit of using a pulsed electron flood gun in order to neutralize the insulating surfaces. In that case, the secondary ion extraction is pulsed and applied only during, and just after the primary ion pulses. Then, after each primary ion pulse the secondary ion extraction is grounded in order to enable the arrival of a “rain” of electrons onto the sample surface which can neutralize it. These electrons emitted from a pulsed electron gun irradiate the surface at a very low energy of a few tens of eV. In most experiments, one can assume that the electron dose density is too low to induce damage. Nevertheless, in cases where acquisition times are very long, the surface modification induced by the electron flood gun would not be negligible.[38]

Cluster ions sources: gold and bismuth LMIGs and fullerenes

There are principally two kinds of cluster ion source available for TOF-SIMS mass spectrometers. The first are derived from LMIGs and produce metal clusters of gold or bismuth. The second are electron impact sources that deliver SF_5^+ and now fullerene ion beams. Figure 2 shows a schematic view of a LMIG emitter. This point source, which is characterized by a very high brightness, can produce submicron focused ion beams. Originally operated with gallium, which is liquid at room temperature, it was subsequently adapted to tin,[39] gold[14] and bismuth.[40] These metals, some of which are mixed in alloys to lower the melting point to a few hundred °C (from 1064 °C for pure gold to 370 and 356°C for the gold-silicon and gold-germanium eutectic alloys, respectively), need to be warmed in order to be liquid in the source. The liquid metal flows from a small reservoir to a needle where it forms a sharp apex. With a high voltage applied between the tip and the extractor, a Taylor cone is generated from which ions are emitted. These ions are mainly monatomic singly charged species, but for metals like gold and bismuth, doubly charged ions and clusters are also formed. The cluster ion beams have intensities that are lower than those of monatomic beams. As an example, Figure 3 gives the relative intensities of the different 25 keV energy cluster ions emitted from a LMIG filled with Au or Bi, respectively.[40] The higher intensities obtained for bismuth compared to gold can be explained in part by the difference between the first and second ionisation potentials of these two metals (1^{st} ionisation potential 9.2 eV for Au_1, 7.3 eV for Bi_1, 2^{nd} ionisation potential 20.5 eV for Au_1 and 16.7 eV for Bi_1) and in part by the lower melting point of pure Bi (271°C) than for Au eutectic alloys. Compared to gold clusters, bismuth clusters, which are more easily emitted (lower ionisation potentials leading to higher emission probabilities), have

lower radial and axial initial energy distributions and are, thus, easier to focus. This last point is observed in reference 40 in which the author reports a smaller focus diameter with the bismuth ion source (spot sizes reaching 100 nm for Bi_3^{2+}) than with the gold one (spot sizes equal to or greater than 200 nm for Au_3^+).

Since the cluster LMIGs emit DC beams containing several kinds of ions (mainly Au^+, Au_2^+ and Au_3^+ for gold, or Bi^+, Bi_2^+, Bi_3^+, Bi_3^{2+}, Bi_4^+, Bi_5^+, Bi_5^{2+}, Bi_6^+ and Bi_7^+ for bismuth), the beams must not only be pulsed but the primary ion must also be mass selected. This mass selection can be accomplished either with a Wien filter or a dual set of deflection plates. Both systems have specific advantages and drawbacks. The Wien filter is capable of a high transmission but suffers from poor resolution and does not eliminate the need for a blanking plate to pulse the beam. The double blanking plates, of which a schematic view is shown in Figure 4, have a better resolution but a lower transmission. Ions of different mass-to-charge ratios fly at different velocities. By placing a second plate operating at a controlled time delay after the first one, ions corresponding to a particular *m/z* can be precisely selected. In order to ensure good mass resolution for the TOF-SIMS spectrometer, a pulse of ions arriving at the sample must have a very short duration, ~1 ns or less. The simplest way is to produce very short pulses with the deflection plates. Unfortunately, such short pulses have relatively poor intensities, which consequently increase the acquisition time. In addition, the energy spread of the primary ions, although small, causes the pulse duration to increase as the primary ions fly from the deflection plates to the sample surface. Consequently, the pulsed primary ion beams need to be bunched by variable electrostatic fields in order to achieve pulse durations at the sample shorter than 1 nsec (without bunching, pulse durations can be several tens of nanoseconds). For a given ion mass-to-charge ratio and

energy, the pulse duration corresponds directly to the spatial extent of the pulse. It is possible, therefore, to shorten this pulse in time by compressing the ion packet in space. A bunching device is made with two plates, each with an aperture on the beam axis. These plates are separated by a distance greater than the spatial extent of the ion pulse. While the ion pulse is flying between the two plates, a voltage is applied to the rear plate in order to accelerate the ions. The ions at the rear of the pulse, which were originally the slowest, are accelerated over a greater distance than the ions at the front of the pulse, which were originally the fastest; consequently, the ions at the rear acquire speeds slightly greater than those at the front of the pulse and, thus, catch up with the latter at some position downstream of the buncher.

Fullerene ion sources, which are generally electron impact ion sources, are also available for TOF-SIMS mass spectrometers.[40,41] C_{60} is first evaporated and ionized through collisions with electrons; depending on the operating conditions, C_{60}^{+} and C_{60}^{2+} ions can be extracted. These ion sources also require primary ion mass selection. Unfortunately the brightness of these ion sources is much lower than for LMIGs, and the ions can be only focused with a reasonable intensity to several micrometers. Although these fullerene ion beams look extremely promising when only taking into account the incomparable secondary ion efficiency of the C_{60}^{+} ions,[29,40,41,42] their performance for imaging purposes is lower than that of cluster LMIGs in terms of focus and intensity. In the following, only the gold or bismuth cluster ion sources will be considered.

Yields, damage, efficiency and useful lateral resolution

In order to compare the efficiency for imaging purposes of the different cluster primary ions, the following quantities can be measured directly from biological tissue sections: secondary ion emission yield *Y*, disappearance cross section σ, secondary ion generation efficiency *E*, specific data rate *R*, and useful lateral resolution δL. These parameters are defined as follows:[43,44]

i – Secondary ion emission yield *Y* is calculated as the area of the peak of interest (number of detected ions) divided by the number of primary ions having impinged the surface during the acquisition of a spectrum.

ii - Disappearance cross section σ is the mean area damaged by one primary ion and depends on the respective secondary ion species under consideration in accordance with the expression $N(t) = N(t=0).exp(-\sigma It/Ae)$ where $N(t)$ is the number of detected particles at time t; $N(t=0)$ is the number of detected particles at time 0; I is the primary ion current; A is the bombarded area; and e is the elemental charge.

iii - Secondary ion efficiency *E* is given by $E = Y/\sigma$ where *E* is the number of detected secondary ions of a given species per damaged area.

iv – Specific Data Rate for the species X is defined as $R(\mathrm{X}) = Y_{\mathrm{X}} I_{\mathrm{X}}$. It is named specific because it depends on both the primary and secondary ions. This parameter is particularly important for large area analysis, while the secondary ion efficiency accounts more for small areas.

v – Relative Specific Data Rate is given by $R_{\mathrm{Bi}_1^+}(\mathrm{X}) = \frac{Y_{\mathrm{X}} I_{\mathrm{X}}}{Y_{\mathrm{Bi}_1^+} I_{\mathrm{Bi}_1^+}}$. $R_{\mathrm{Bi}_1^+}(\mathrm{X})$ is calculated relative to Bi_1^+. The higher the value the better is the primary ion species *X* suited for imaging.

vi – Useful lateral resolution ΔL is the side of the minimum square area in which N secondary ions of a given mass can be desorbed and detected. This corresponds to the area ΔL^2 which has to be damaged to record N secondary ions. For $N = 4$ one obtains $\Delta L = (4/E)^{1/2}$.

Y, E and R need to be maximized to optimize the primary ion capabilities, while σ and ΔL must be minimized.

Data exist in the literature that compare the yields, damage cross section and efficiencies between Ga^+, C_{60}^+, Au^+, Au_3^+ and Bi_3^{2+} ions striking test samples like Irganox, gramicidin or selected polymers.[40,41,45] Those data have been generally obtained from monolayer or sub-monolayer samples that have been spincoated onto silicon wafers. Although this enables some reproducibility in the comparisons, those data are far from representing real biological samples such as a thin tissue sections. Nevertheless a general trend can be found, with primary ion efficiencies scaling as follows: $Ga^+ < Au^+$ (or Bi^+) $< Au_3^+$ (or Bi_3^+) $< Bi_3^{2+} < C_{60}^+$.

Table 1 shows the average values of Y, σ, E, R, and ΔL measured for $[M\text{-}H]^+$ secondary ions of cholesterol (*m/z* 385) due to different bismuth clusters (Bi_1^+, Bi_3^+, and Bi_5^{2+}) impinging directly onto two positions of the surface of a rat brain section. The values were measured according to the procedure already used by Touboul *et al* when comparing Au^+ and Au_3^+ ions.[15] The yield increases by a factor of 8.4 when switching from Bi_1^+ to Bi_3^+ while the disappearance cross section only rises by a factor of 1.6; this results in an efficiency enhancement of 5. Therefore, Bi_3^+ bombardment is superior to Bi_1^+ bombardment when aiming at low detection limits. The useful lateral resolutions are the best (377 nm) for Bi_5^{2+} (compared to ~500 nm for Bi_3^+ and more than 1 μm for Bi_1^+). In order to compare the imaging capabilities of these primary ions, it is necessary

to take also into account the primary ion currents. Indeed, a primary ion beam with the best efficiency but the smallest intensity would not be able to produce secondary ion images in a short time. The parameter *R* takes into account both the secondary ion emission yield and the primary ion current. Due to the fact that the Bi_3^+ ion intensity is about 7 times higher than it is for Au_3^+, a secondary ion image can be recorded using Bi_3^+ in one seventh of the time that would be required using Au_3^+ with the same primary ion dose density; alternatively during equivalent acquisition times, one can record an image with a 7 times greater primary ion dose density. This is particularly important when recording secondary ion images of large areas, such as for an entire rat brain section (more than 3 cm^2) for which it takes rather a long time to reach a primary ion dose density higher than a few 10^9 ions cm^{-2}. Otherwise, for mapping only small areas, on the order of 500x500 μm^2, Bi_5^{2+} ions have a particularly attractive efficiency. It must be noted that the increase of efficiency and the better useful lateral resolution obtained for Bi_5^{2+} ions are not due to the double charge of this projectile, as in the paper of Benguerba *et al*,[14] where it was noticed that the yields were not affected by the charge of the primary ions.

Finally another important parameter is the surface damage generated on the biological tissue. It has been mentioned above that most of the molecules are destroyed close to the projectile track. If, when switching from atomic projectiles to polyatomic ones, the damage would increase as fast as the secondary ion emission, then the efficiency *E*, which is defined as the ratio between the secondary ion emission yield *Y* over the damage cross section σ, would not be better. Fortunately, it has been measured from different kinds of samples that the secondary ion emission yield increases faster than the damage cross section,[40] increasing consequently the efficiency by factors ~20 between

Au_1^+ and Au_3^+ impinging on animal tissue sections.[15] From the damage cross section one can also define what is generally called the static SIMS limit. This parameter is easy to define and to measure with respect to well defined surfaces like those of metals and semi-conductors. It corresponds to the primary ion dose density (PIDD), in ions per square centimeter, necessary to sputter a monolayer of the sample. Then in principle this value is simply the inverse of the damage cross section. If the PIDD is much larger than $1/\sigma$, one should talk about dynamic SIMS. Nevertheless for real biological samples like an animal tissue section, the damage cross section depends on a lot of parameters, such as the nature of the chemical compound studied or the chemical environment of this compound. With atomic projectiles it is generally admitted[46] that the static SIMS limit is $\sim 10^{13}$ ions.cm^{-2}. This value needs to be used with caution when studying real biological samples, with or without cluster projectiles, and it is judicious to irradiate the samples with PIDD lower than this value.

Sample preparation

The incomparable advantage of Cluster TOF-SIMS imaging is that it can be implemented without any preliminary treatment of the sample. The biological tissue section does not need to be washed or coated by any matrix, salt, or metal. As the technique is also not destructive, it preserves the possibility to use the same sample for other imaging techniques like fluorescence microscopy, histochemistry, or even matrix-assisted laser desorption/ionisation imaging. The only requirements are that the compounds of interest must remain in the same position in the sample that existed before it was sectioned, and the section must lie flat for a good secondary ion extraction. The best conditions are the following. The sample must not be altered by any chemical treatment or fixation, such as those often employed for other imaging techniques. After removing an organ from a sacrificed animal or taking a biopsy, the sample must be frozen in liquid nitrogen or in isopentane; however, any chemical fixation must be avoided because most of the chemical fixatives may react with the molecules that can be detected by TOF-SIMS. The biological tissue is first cut at a temperature of ~ -18/20°C in a cryostat. The tissue sections, which have a thickness of 15 μm, are immediately deposited onto a stainless steel plate and kept at -80°C. Other sample holders can be utilized instead of stainless steel, such as a glass plate coated or not by a thin conductive layer, but it appears that the best extraction conditions and consequently the highest sensitivity and mass resolution are obtained when using stainless steel plates. Just before analysis, the plates are warmed to room temperature and dried under vacuum. Under these conditions and on a scale of a few hundred nanometers, no delocalisation is observed for any of the observed compounds regardless of their mass. It is unlikely that compounds such as phospholipids could move, but it is generally feared that light

elements like Na^+ or K^+ can be rapidly delocalized on a nanometer scale. Nevertheless, no such movement of alkaline or organic ions has been observed at the micrometer scale and under the conditions described above. In addition, this sample preparation method is robust, reproducible, easy, and does not limit the lateral resolution.

Some authors have adapted TOF-SIMS preparation methods that were previously utilized for other kind of analysis to biological tissue imaging. It has been shown some years ago that the use of the MALDI matrix 2,5-dihydroxybenzoic acid could strongly enhance the secondary ion emission of peptides. This method which was called "Matrix-enhanced SIMS" (ME-SIMS)[47] has recently been applied to TOF-SIMS imaging.[13] The matrix is very homogeneously deposited onto the biological tissue surface by an electrospray device. This coating method produces very small matrix crystals having a size of a few microns only and enhances the secondary ion emission of ions like those of cholesterol in brain tissues. It also limits the spatial resolution to the size of the crystals, and the signal enhancement could depend on the chemical structure of the secondary ions. In addition, the interpretation of the ME-SIMS spectra can be made complex because of the presence of matrix ion peaks, which could interfere with ion peaks from the sample itself.

Another approach to image improvement takes advantage of the secondary ion yield enhancement that results from cationisation with elements like silver or gold.[48] This technique is well known to enhance the ionisation yields of some compounds, particularly polymers, and has been recently applied by Nygren *et al* to rat kidney sections.[12] In their experiment, a tissue section is coated by a few nanometers of silver. This silver layer is vapour deposited with a thickness controlled by a quartz crystal microbalance. The signal from silver cationized cholesterol ions was sufficiently intense

(the experiments were performed with a Ga^+ primary ion source) to produce an image. Nevertheless the cholesterol ion is the only significant biological compound which was reported, and one must wonder how specific this metal cationisation is. These two methods, ME-SIMS and cationisation, are obviously available only for positive secondary ions. A third method has been developed by Sjövall *et al*. that consists in making an imprint of single cells onto a silver surface and subsequently analysing the imprint by TOF-SIMS.[49] Again, silver cationized cholesterol ions were detected with enough intensity to image it at a submicron spatial resolution. It must be noted that the three methods mentioned above have been used with TOF-SIMS spectrometers which were not equipped with gold or bismuth cluster ion sources, but with gallium LMIGs. The use of a cluster ion source would probably have made it easier to acquire the image because the sample coating or imprint does not seem to be essential. In the meantime for certain cases, these preparation methods can still be used jointly with a cluster LMIG to increase the sensitivity several times over.

Image Acquisition and Processing

Data acquisition

The generation of secondary ion images means mapping the distribution of compounds at the surface of a sample as revealed by the detection of characteristic ions. More precisely, a secondary ion image is an *ion density map*. In order to obtain such data, it is necessary to scan the focused primary ion beam over the sample from a given position to another via a so-called *raster*, which produces a square or rectangular pattern.[50] Each position of this raster is called a *pixel*. From each of these pixels, an entire TOF mass spectrum is recorded. So an acquisition can contain as many secondary ion images as peaks in the spectra. The data acquisition consists in the creation of a volume whose dimensions are *x* and *y*, the two geometric dimensions of the sample, and *m/z* the mass to charge ratio of the secondary ions. The projection of this (*x*, *y*, *m/z*) volume onto the *m/z* axis is the global spectrum, without any spatial information, while the projection onto the (*x*, *y*) plane is the global image, sometimes called total ion image in the literature. A slice along a given *m/z* value is the secondary ion image corresponding to this *m/z* value.

In TOF-SIMS instruments, there are two ways to manage the raster of the sample surface, both of which are illustrated in Figure 5. In the first, the sample is motionless while the primary ion beam moves over it from one pixel position to the next (Figure 5A). This is particularly easy, and because it is achieved with electrostatic deflection plates, it can be driven with voltages to a precision better than 1 ppm. If the beam focus is smaller than the pixel size, then it itself must be rastered inside of each pixel. The spatial resolution is obviously limited to the beam focus. The size of the image that can be acquired with this procedure is limited to the field of the secondary ion extraction

optics. In most instruments, this size is of the order of 500x500 μm^2. While the axis of the secondary ion extraction optics is generally perpendicular to the sample surface, the axis of the primary ion beam column cannot be. So in one direction, the primary ion path is longer to one edge of the raster surface than to the opposite edge. In addition, the secondary ions need to traverse a longer path when produced at the edge of the surface than when produced at the centre. Both of these path differences produce small time-of-flight differences that limit the time resolution and hence the mass resolution. For images having a surface greater than the field of the secondary ion extraction optics, the primary ion beam is not moved but rather the sample holder is moved step by step from one pixel to the other (Figure 5B). This requires that the mechanical motors to be extremely precise and reproducible, i.e. do not shift or generate hysteresis when changing from one direction to the another (backlash). This method makes it possible to record secondary ion images having a size of several square centimetres. In this case, the pixel size is generally much larger than the primary ion beam spot, and the beam is rastered inside each pixel in order to avoid undersampling during the data acquisition.[50] Regardless of whether the area to be analysed is large or small, the sample surface must be flat and always perpendicular to the axis of the secondary ion optics. Otherwise, height differences would translate into time-of-flight differences that would severely reduce the mass resolution.

The signal intensity of a given ion emitted from a given pixel is a function of the concentration of the corresponding compound in the sample's surface. Despite this fact, the nature of this functionality is too complex to describe analytically in any given situation because, as is well known in SIMS, the emission of ions is strongly dependent on the surrounding compounds. In other words the emission can be unpredictably

disturbed – enhanced of diminished – by matrix effects. Therefore, the present method can be only regarded as one for determining the relative composition of the mapped compounds, not one for absolute quantitative measurements.

Another consideration that must be taken into account for biological tissue imaging is the number of molecules available in a pixel. The primary ion dose density must not exceed the so-called static SIMS limit. This limit corresponds in principle to the sputtering, or to the damage, of the topmost monolayer at the surface. While the static SIMS limit is generally admitted[46] to be situated around a primary ion dose density of 10^{13} ions cm^{-2}, it seems (see above) that the limit is lower for organic compounds originating from tissue samples, especially when the primary ions are clusters. During acquisition of an image from a biological tissue, it is strongly recommended that the static SIMS limit not be exceeded. The composition of the surface could otherwise be modified. As a consequence, the limit on the primary ion dose density places in turn an upper limit on the count rates. Typical values can be deduced from Table 1, bearing in mind that the useful lateral resolution ΔL is measured for an estimated number of counts per pixel equal to 4. This value of 4 counts per pixel appears in general to be the minimum value that enables an ion image to be easily read and analyzed by the human eye.

The acquisition time needs also to be considered. The primary ion beam can be pulsed with a frequency, or a repetition rate that can be several tens of kiloHertz. This frequency is limited by the maximum m/z value that needs to be recorded. The $(m/z)_{max}$ value corresponds to a total time – the time-of-flight of the ions – between one pulse and the next. Indeed, a second primary ion pulse cannot be sent to the sample before ions of $(m/z)_{max}$ arrive at the detector because light secondary ions from the succeeding

pulse could produce parasitic peaks in the spectrum. As an example, with *m/z* of the secondary ions equal to 1500, the length of the field free path equal to 2 m, and a kinetic energy equal to 2 keV, the time of flight would be equal to ~115 μsec. Hence, the maximum frequency of the primary ion pulsation in this case would be ~8 kHz. A number of other factors can also limit the acquisition time. First would be the time necessary to move the sample from one position to another when the image size dictates the use of a mode in which the sample holder is moved. The mechanical motors need to be very fast. The electronics of the data acquisition can also introduce dead times that need to be minimized in order not to reduce the speed of data acquisition. Last of all, the sample area can strongly influence the data acquisition time. If it takes 0.7 second to record an image of 256x256 pixels over a surface of 50x50 μm^2 with a primary ion intensity of 0.5 pA at 8 kHz (9.10^{10} ions cm^{-2}), it would take 70 seconds for the same primary ion dose density on a surface of 500x500 μm^2, and 7200 seconds (2 hours) on a surface of 5000x5000 μm^2.

Such images having 256x256 pixels may correspond to a huge amount of data since an individual mass spectrum is associated with each of the 65 536 pixels. Generally the files corresponding to such an acquisition are greater than several hundred megabytes and, in some cases, can reach more than 2 gigabytes. The computer which controls the data acquisition and recording needs to run with a fast processor, large RAMs, and big hard disks in order not to limit the speed of acquisition.

Image examples are given in Figures 6, 7, and 9. These three acquisitions have been performed in three steps on the same rat brain tissue section. Table 2 summarizes the parameters that characterize these three figures. The first two sets of images were obtained in positive (Figure 6) and in negative (Figure 7) ion modes with moderate Au_3^+

primary ion dose densities of 4.10^8 ions cm^{-2}, each over the whole surface of the rat brain section. In these first two cases, the number of pixels was 256x256; the pixel size was 62.5x62.5 μm^2; and the acquisition was made according to the procedure of Figure 5B by moving the sample holder. The third image (Figure 9) was recorded from a small area (500x500 μm^2) of the total shown in Figure 8. In this last case the number of pixels was 256x256; the pixel size was 1.95x1.95 μm^2; and the Au_3^+ primary ion dose density was $6.5.10^{10}$ ions cm^{-2}. These three images show a lot of positive and negative secondary ions, which are fragment ions but also molecular ions, with masses ranging from *m/z* 23 to ~900. Some of these ions enable recognition of particular regions of the brain with an excellent precision.[15,16,51] Imaging mass spectrometry makes it possible to correlate different compounds by cospatial or antispatial localisation.

Digital image processing

At the end of the acquisition of the mass spectrometric images, the data are generally saved as a raw file – the (*x, y, m/z*) volume described above – from which the images can be extracted. The most convenient way to extract these images is to begin working with the two projections, *i.e.* the total spectrum and the total ion image. From the first one, it is possible to define a list of *m/z* intervals from which images can be generated. These intervals can correspond to single *m/z* values or to broader ranges including several ions. Through inversion of the total ion image, it is inversely possible to define a contour from which the mass spectrum of a specific region can be generated. This makes it possible to compare the spectra of different areas with the investigated biological tissue surface. Furthermore, a lot of image processing methods can be applied to the images in order to facilitate understanding the tissue compound content: smoothing, averaging, operation between images such as normalisation between two

images, sum, subtraction, and colour overlays. Since color perception can vary from one reader to another, several color palettes must be available in order to facilitate the viewing the image.

An example of data processing is given in Figure 10. An image recorded with an extremely high lateral resolution of only 218 nm is compressed and averaged in order become more easily readable. Particularly, it is shown that the localisation of some secondary ions would be hardly distinguishable without this data treatment.

Another important data processing method is the so-called principal component analysis (PCA). Most image processing software include this function. While a detailed description of PCA is beyond the scope of this review, one should mention that this data analysis method can in some cases be terrific for extracting spatial information and correlations.[52]

Compatibility between SIMS and MALDI mass spectrometry imaging methods

Usually the primary ion dose density which is necessary to acquire images such as those of Figures 6, 7 and 9 are well below the static SIMS limit, which is somewhere in the range of 10^{12} to 10^{13} ions cm^{-2}. The total primary ion dose density applied to record these three images was $8x10^{8}$ ions cm^{-2} over the entire section (Figures 6 and 7) and $6.5x10^{10}$ ions cm^{-2} over the much smaller area (Figure 9). Furthermore, no sample coating or washing was necessary to perform these three acquisitions which took a few hours to be recorded. Hence, the sample can be considered still available for a MALDI-TOF imaging experiment.[4,5,50] It is possible to coat the surface with a MALDI matrix like sinapinic acid, and to irradiate it with an UV laser in order to record a MALDI image. This exciting possibility is illustrated in Figure 11 where the sample irradiated for the Figures 6, 7 and 9 has been mapped using MALDI imaging. The MALDI image

of a peptide at an average *m/z* 6756 shows a very nice, complementary localisation with the secondary ions of cholesterol used to record the SIMS image.

Applications in life sciences: lipidomics, drug metabolism, genetic diseases

Until recently, TOF-SIMS imaging was suffering from the poor secondary ion production efficiency of the traditional Gallium or Indium liquid metal ion guns. The introduction of LMIGs constitutes an important breakthrough in this regard; however, this advance is so recent that very few applications to life sciences have been made. Nevertheless, the field is extremely promising. Nygren *et al* have coated a rat kidney tissue section with silver and have been able to map the distribution of cholesterol ions.[12] The cholesterol signal showed a high concentration in the nuclear areas of the epithelial cells and a lower concentration over areas representing the basal lamina of renal tubules. A more diffuse distribution of cholesterol was also found over areas representing the cytoplasm or plasma membrane of the epithelial cells. Using a gold cluster LMIG, Touboul *et al* have studied the localisation of cholesterol, vitamin E and fatty acids in the surroundings of degenerating and regenerating mouse muscular cells suffering from Duchenne muscular dystrophy.[37] Beyond these two applications, the mass range, which is now accessible with TOF-SIMS imaging using a cluster LMIG, combined with the micron and sub-micron spatial resolution and the compatibility with subsequent MALDI imaging makes the technique particularly promising in searches for biomarkers of diseases. Very fine changes in lipid metabolism can be observed at the cell level. A parallel proteomics study performed jointly with MALDI imaging, or at least MALDI profiling albeit at a much poorer lateral resolution, will almost certainly reveal useful information in the near future about a number of genetic and neurodegenerative diseases. Finally, the study of drug metabolism at the cell level can be eventually contemplated with TOF-SIMS using clusters.

Current status, future developments

The analysis of biological tissue by TOF-SIMS imaging with cluster ion sources is possible for a mass range extending to about one thousand Daltons. In one single analysis, a number of different compounds can be mapped with subsequent spatial and antispatial correlations. The possibility of performing a MALDI imaging experiment on the same sample after SIMS imaging opens the possibility of investigating a very wide mass range, from small ions (lipids, drug metabolites) up to peptides and proteins. Although the recent application of cluster LMIGs seems to push TOF-SIMS towards life science applications, it must be noted that the mass range remains limited, and the observed secondary ions seem to come more often from hydrophobic molecules than others. The combination of new biological tissue treatment or coating in conjunction with the use of the cluster ion probes can be expected in the future to further extend the sensitivity of TOF-SIMS towards higher masses and also to less specific compounds. Other kinds of cluster ion sources already exist; these devices produce clusters that are expected to be more efficient than the gold or bismuth LMIGs. Specifically, these sources are, on the one hand, the fullerene ion sources[41] and, on the other hand, LMIGs operated under very special conditions that emit very large cluster ions like Au_{400}^{4+} clusters.[53] Unfortunately, these ion sources cannot yet deliver the focused ion beams on a sub-micron scale that are standard with the gold or bismuth LMIGs. Nevertheless, as these ion beams deposit a large amount of their energy very close to the surface, they are expected to be extremely efficient for surface sputtering without strongly damaging the deeper layers. Hence, one can imagine that these ion sources, C_{60} or heavy gold cluster, could be utilized for organic surface sputtering, thereby opening a new field of dual source depth profiling directly into a biological tissue section.

Although the speed of the data acquisition is higher than for MALDI imaging experiments, further improvements are still expected in this field, particularly for large surface analysis of several square centimeters, where reaching a primary ion dose density of 10^9 ions cm^{-2} can take several hours. As it is not possible to increase the pulse repetition rate without limiting the recorded mass range, it is necessary to increase both the primary ion currents and the computer and motor performances in order to shorten this kind of data acquisition.

As the MALDI and cluster SIMS imaging methods can be successively utilized on the same sample, data correlation software must be developed. These data processing methods should be able to recognize and correlate the two kinds of images while also being able to import any kind of image obtained from other microscopic surface mapping.

Finally, the mass assignments need in most cases a confirmation by a determination of the compound structure. Therefore MS/MS methods cannot remain disregarded by the TOF-SIMS imaging techniques. Post-source decay measurements[54] can in the near future be considered without major modifications of the reflectron TOF analyzers.

Acknowledgements

D.T. is indebted to the Institut de Chimie des Substances Naturelles (CNRS) for a Ph.D. research fellowship. The authors thank Allan Medeiros for his invaluable help in the development of the data processing softwares and D.F. Barofsky for reading and improving the manuscript.

References

[1] Castaing R, Slodzian G. Microanalyse par émission ionique secondaire. J. Microsc. 1962; **1**: 395.

[2] Benninghoven A, Loebach, E. Tandem mass spectrometer for secondary ion studies. Rev. Sci. Instrum. 1971; **42**: 49.

[3] Chait BT, Standing KG. A time-of-flight mass spectrometer for measurement of secondary ion mass spectra. Int. J. Mass Spectrom. Ion Phys. 1981; **40**: 185

[4] Caprioli RM, Farmer TB, Gile J. Molecular imaging of biological samples: Localization of peptides and proteins using MALDI-TOF MS. Anal. Chem. 1997; **69**: 4751.

[5] Stoeckli M, Chaurand P, Hallahan DE, Caprioli RM. Imaging mass spectrometry: A new technology for the analysis of protein expression in mammalian tissues. Nat. Med. 2001; **7**: 493.

[6] Karas M, Bachmann D, Bahr U, Hillenkamp F. Matrix-assisted ultraviolet laser desorption of non-volatile compounds. Int. J. Mass Spectrom. Ion Processes. 1987; **78**: 53

[7] Reyzer ML, Hsieh Y, Ng K, Korfmacher WA, Caprioli RM. Direct analysis of drug candidates in tissue by matrix-assisted laser desorption/ionization mass spectrometry. J. Mass Spectrom. 2003; **38**: 1081.

[8] Pacholski ML, Cannon DM, Ewing AG, Winograd N. Static time-of-flight secondary ion mass spectrometry imaging of freeze-fractured, frozen-hydrated biological membranes. Rapid Commun. Mass Spectrom. 1998; **12**: 1232.

[9] Sudraud P, Van de Walle J, Colliex C, Castaing R. Contribution of field effects to the achievement of higher brightness ion sources. Surf. Sci. 1978; **70**: 392.

[10] Pacholski ML, Winograd N. Imaging with mass spectrometry. Chem. Rev. 1999; **99**: 2977.

[11] Belu AM, Graham DJ, Castner DG. Time-of- flight secondary ion mass spectrometry: techniques and applications for the characterization of biomaterial surfaces. Biomaterials. 2003; **24**: 3635.

[12] Nygren H, Malmberg P, Kriegeskotte C, Arlinghaus HF. Bioimaging TOF-SIMS: localization of cholesterol in rat kidney sections. FEBS Letters. 2004; **566**: 291.

[13] McDonnel LA, Piersma SR, Marten Altelaar AF, Mize TH, Luxembourg SL, Verhaert PDEM, van Minnen J, Heeren RMA. Subcellular imaging mass spectrometry of brain tissue. J. Mass Spectrom. 2005; **40**: 160.

[14] Benguerba M, Brunelle A, Della-Negra S, Depauw J, Joret H, Le Beyec Y, Blain MG, Schweikert EA, Ben Assayag G, Sudraud P. Impact of slow gold cluster on various solids: Nonlinear effects in secondary ion emission. Nucl. Instrum. Methods Phys. Res. B 1991; **62**: 8.

[15] Touboul D, Halgand F, Brunelle A, Kersting R, Tallarek E, Hagenhoff B, Laprévote O. Tissue molecular ion imaging by gold cluster ion bombardment. Anal. Chem. 2004; **76**: 1550.

[16] Sjövall P, Jausmaa J, Johansson B. Mass spectrometric imaging of lipids in brain tissue. Anal. Chem. 2004; **76**: 4271.

[17] Luxembourg SL, Todd HM, McDonnel LA, Heeren RMA. High Spatial Resolution Mass Spectrometric Imaging of Peptide and Protein Distributions on a Surface. Anal. Chem. 2004, **76**: 5339.

[18] Urbassek HM. Status of cascade theory. in ToF-SIMS - Surface Analysis by Mass Spectrometry; Vickerman JC, Briggs D. Eds.; SurfaceSpectra and IM Publications: Manchester and Chichester, 2001, 139.

[19] Sigmund P. Theory of Sputtering. I. Sputtering Yield of Amorphous and Polycrystalline Targets. Phys. Rev. 1969; **184**: 383 & 1969; **187**: 768.

[20] Ziegler JF, Biersack JP, Littmark U. The Stopping and Ranges of Ions in Solids, Pergamon Press, New York, 1985. www.srim.org

[21] Sigmund P, Claussen C. Sputtering from elastic-collision spikes in heavy-ion-bombarded metals. J. Appl. Phys. 1981; **52**: 990.

[22] Bitensky IS, Parilis ES. Shock wave mechanism for cluster emission and organic molecule desorption under heavy ion bombardment. Nucl. Instrum. Methods. Phys. Res. B 1987 ; **21** : 26.

[23] Brunelle A, Della-Negra S, Depauw J, Jacquet D, Le Beyec Y, Pautrat M, Baudin K, Andersen HH. Enhanced secondary ion emission under gold cluster bombardment with energy from keV to MeV per atom. Phys. Rev. A 2001; **63**: 022902.

[24] Andersen HH, Bay HL. Nonlinear effects in heavy-ion sputtering. J. Appl. Phys. 1974; **45**: 953.

[25] Andersen HH, Bay HL. Heavy-ion sputtering yields of gold: Further evidence of nonlinear effects. J. Appl. Phys. 1975; **46**: 2416.

[26] AppelHans DA, Delmore, JE. Comparison of polyatomic and atomic primary beams for secondary ion mass spectrometry. Anal. Chem. 1989; **61**: 1087.

[27] Colla TJ, Aderjan R, Kissel R, Urbassek HM. Sputtering of Au (111) induced by 16-keV Au cluster bombardment: spikes, craters, late emission and fluctuations. Phys. Rev. B 2000; **62**: 8487.

[28] Bolbach G, Viari A, Galera R, Brunot A, Blais JC. Organic film thickness effect in secondary ion mass spectrometry and plasma desorption mass spectrometry. Int. J. Mass Spectrom. Ion Processes. 1992; **112**: 93

[29] Boussofiane-Baudin K, Bolbach G, Brunelle A, Della-Negra S, Håkansson P, Le Beyec Y. Secondary ion emission under cluster impact at low energies (5-60 keV); Influence of the number of atoms in the projectile. Nucl. Instrum. Methods. Phys. Res. B 1994;, **88**: 160.

[30] Guilhaus M. Principles and instrumentation in time-of-flight mass spectrometry. J. Mass Spectrom. 1995; **30**: 1519.

[31] Uphoff A, Grotemeyer J. The secrets of time-of-flight mass spectrometry revealed. Eur. J. Mass Spectrom. 2003; **9**: 151.

[32] Cotter RJ. The new time-of-flight mass spectrometry. Anal. Chem. 1999; **71**: 445A.

[33] Cotter RJ. Time-of-Flight Mass Spectrometry, American Chemical Society, Washington DC, 1997.

[34] Karataev VI, Mamyrin BA, Shmikk DV. New method for focusing ion bunches in time-of-flight mass spectrometers, Soviet Phys. Tech. Phys. 1972; **16**: 1177.

[35] Mamyrin BA, Karataev VI, Shmikk DV, Zagulin VA. The mass reflectron, a new non-magnetic time-of-flight mass spectrometer with high resolution. Sov. Phys. JETP. 1973; **37**: 45.

[36] Gilmore IS, Seah MP. Ion detection efficiency in SIMS:dependencies on energy, mass and composition for microchannel plates used in mass spectrometry. Int. J. Mass Spectrom. 2000; **202**: 217.

[37] Touboul D, Brunelle A, Halgand F, De La Porte S, Laprévote O. Lipid imaging by gold cluster time-of-flight - secondary ion mass spectrometry: Application to Duchenne muscular dystrophy., J. Lipid. Res. 2005; **46**: 1388.

[38] Gilmore IS, Seah MP. Electron flood gun damage in the analysis of polymers and organics in time-of-flight SIMS. Appl. Surf. Sci. 2002; **187**: 89.

[39] Barofsky DF, Jiang LF, Yen TY. A novel, pulsed, liquid metal ion time–of–flight mass spectrometer. in Ion Formation from Organic Solids (IFOS V); Hedin A, Sundquist BUR, Benninghoven A. Eds; John Wiley & Sons: Chichester, England, 1990, 87.

[40] Kollmer F. Cluster primary ion bombardment of organic materials. Appl. Surf. Sci 2004, **231-232**; 153.

[41] Weibel D, Wong S, Lockyer N, Blenkinsopp P, Hill R, Vickerman JC. A C_{60} Primary ion beam system for time of flight secondary ion mass spectrometry: Its development and secondary ion yield characteristics. Anal. Chem. 2003; **75**: 1754.

[42] Winograd N. The magic of cluster SIMS. Anal. Chem. 2005; **77**: 143A.

[43] Kötter F; Benninghoven A. Secondary ion emission from polymer surfaces under Ar^+, Xe^+ and SF_5^+ ion bombardment. Appl. Surf. Sci. 1998; **133**: 47.

[44] Touboul D, Kollmer F, Niehuis E, Brunelle A, Laprévote O. Improvement of biological TOF-SIMS imaging with a bismuth cluster ion source. J. Am. Soc. Mass Spectrom., in press.

[45] Nagy G, Gelb LG, Walker AV, An investigation of enhanced secondary ion emission under Au_n^+ (n = 1–7) bombardment. J. Am. Soc Mass Spectrom. 2005; **16**: 733.

[46] Vickerman JC. TOF-SIMS – an overview. in ToF-SIMS - Surface Analysis by Mass Spectrometry; Vickerman JC, Briggs D. Eds.; SurfaceSpectra and IM Publications: Manchester and Chichester, 2001, 1.

[47] Wu KJ, Odom RW. Matrix-enhanced secondary ion mass spectrometry: A method for molecular analysis of solid surfaces. Anal. Chem. 1996; **68**: 873.

[48] Delcorte A, Bour J, Aubriet F, Muller JF, Bertrand P. Sample metallization for performance improvement in desorption/ionization of kilodalton molecules: Quantitative evaluation, imaging secondary ion MS, and laser ablation. Anal. Chem. 2003; **75:** 6875.

[49] Sjövall P, Lausmma J, Nygren H, Carlsson L, Malmberg P. Imaging of membrane lipids in single cells by imprint-imaging time-of-flight secondary ion mass spectrometry. Anal. Chem. 2003; **75**: 3097.

[50] Todd PJ, Schaaff TG, Chaurand P, Caprioli RM. Organic ion imaging of biological tissue with secondary ion mass spectrometry and matrix-assisted laser desorption/ionization. J. Mass Spectrom. 2001; **36**: 355.

[51] The rat brain in stereotaxic coordinates, 4th edition, G. Paxinos & Ch. Watson; Academic Press, London, 1998.

[52] Tyler BJ. TOF-SIMS Image analysis. in ToF-SIMS - Surface Analysis by Mass Spectrometry; Vickerman JC, Briggs D. Eds.; SurfaceSpectra and IM Publications: Manchester and Chichester, 2001, 475.

[53] Tempez A, Schultz JA, Della-Negra S, Depauw J, Jacquet D, Novikov A, Le Beyec Y, Pautrat M, Caroff M, Ugarov M, Bensaoula H, Gonin M, Fuhrer K, Woods A. Orthogonal time-of-flight secondary ion mass spectrometric analysis of peptides using large gold clusters as primary ions. Rapid Commun. Mass Spectrom. 2004; **18**: 371.

[54] Spengler B, Kirsch D, Kaufmann R, Cotter RJ. Metastable decay of peptides inmatrix-assisted laser-desorption mass spectrometry. Rapid commn. Mass Spectrom. 1991; **5**: 198.

Figure captions:

Figure 1: Secondary ion emission yield of the negative secondary ion of the phenylalanine $[M-H]^-$ *m/z* 164.2, as a function of the velocity per mass unit of the different Au_n^+ (n = 1-5) projectiles. A strong nonlinear enhancement is observed. Reprinted from Reference 14, Copyright 2005, with permission from Elsevier.

Figure 2: Schematic view of a LMIG emitter.

Figure 3: Primary ion currents for Au and Bi clusters as a function of cluster size and charge; the currents are normalized to the values of ~1 pA for Au_1^+ and Bi_1^+. Reprinted from Reference 40, Copyright 2005, with permission from Elsevier.

Figure 4: Schematic view of dual blanking plates that ensure both pulsation of the DC primary ion beam and mass selection among the different cluster ions emitted.

Figure 5: Two ways of rastering the sample surface with the primary ion beam. In A, the beam is rastered with electrostatic plates over the sample surface and the sample holder is not moving. In B, the sample holder is moving from one position (pixel) to the next, and the primary ion beam is only rastering inside the pixel. The first method accounts for small surface analyses that do not exceed the field of the secondary ion extraction optics while the second is adapted for large surface analyses.

Figure 6: Rat brain tissue section: images of several positive secondary ions (Na^+; *m/z* 23, K^+; *m/z* 39, choline; *m/z* 86, phosphocholine head group; *m/z* 184, cholesterol $[M+H-H_2O]^+$; *m/z* 369, Vitamin E; *m/z* 430, phospholipids; mean *m/z* 769; total ion image). Primary ions Au_3^+ 25 keV, 4.10^8 ions cm^{-2}, area 16x16 mm^2, 256x256 pixels, pixel size 62.5x62.5 μm^2. The maximum number of counts *mc* corresponds to the amplitude of the colour scale: [0, mc], and *tc* is the total number of counts recorded for

the specified *m/z* (it is the sum of counts in all the pixels). Acquisition made according to the procedure of Figure 5B by moving the sample holder.

Figure 7: Rat brain tissue section: images of several negative secondary ions ($[PO_3]^-$; *m/z* 79, C16 fatty acids; mean *m/z* 255, C18 fatty acids; mean *m/z* 283, cholesterol $[M-H]^-$; *m/z* 385, triglyceride ions; mean *m/z* 892; total ion image). Primary ions Au_3^+ 25 keV, 4.10^8 ions cm^{-2}, area 16x16 mm^2, 256x256 pixels, pixel size 62.5x62.5 μm^2. These images have been obtained from the same area of the same rat brain tissue section as for Figure 6. The maximum number of counts *mc* corresponds to the amplitude of the colour scale: [0, mc], and *tc* is the total number of counts recorded for the specified *m/z* (it is the sum of counts in all the pixels). Acquisition made according to the procedure of Figure 5B by moving the sample holder.

Figure 8: A: Zoom made by software of the *m/z* 86 image in Figure 6 showing an area (white and dashed square) where the high resolution image of Figure 9 is recorded. **B:** optical image of the rat brain tissue section showing the area (white square 500x500 μm^2) where the image of Figure 9 is recorded.

Figure 9: Rat brain tissue section: images of several positive secondary ions (Na^+; *m/z* 23, K^+; *m/z* 39, choline; *m/z* 86, phosphocholine head group; *m/z* 184, cholesterol $[M+H-H_2O]^+$; *m/z* 369, Vitamin E; *m/z* 430, phospholipids; mean *m/z* 774; total ion image). Primary ions Au_3^+ 25 keV, $6.5.10^{10}$ ions cm^{-2}, Area 500x500 μm^2, 256x256 pixels, pixel size 1.95x1.95 μm^2. These images have been obtained from the same rat brain tissue section as for Figures 6 and 7. The maximum number of counts *mc* corresponds to the amplitude of the colour scale: [0, mc], and *tc* is the total number of counts recorded for the specified *m/z* (it is the sum of counts in all the pixels).

Acquisition made according to the procedure of Figure 5A by moving only the primary ion spot.

Figure 10: Examples of data processing. First line: positive secondary ion images of phosphocholine head group; *m/z* 184, cholesterol $[M-H]^+$; *m/z* 385 and Vitamin E; *m/z* 430. Primary ions Bi_3^+, 25 keV, 5.10^{12} ions.cm^{-2}, area 55.7x55.7 μm^2, 256x256 pixels, pixel size 218x218 nm^2. Second line: the images of the first line have been compressed to 128x128 pixels. Each pixel is the sum of 4 adjacent pixels. Third line: the images of the second line have been processed using an averaging method. Each pixel is averaged taking into account the surrounding pixels. Fourth line: two-color overlay between 2 of the processed images on the third line.

Figure 11: Illustration of the compatibility between MALDI-TOF and Cluster TOF-SIMS mass spectrometry imaging. **A:** Cluster TOF-SIMS image of the cholesterol ion obtained from a rat brain tissue section (same as in Figure 6). **B:** MALDI-TOF image of a peptide at *m/z* 6756. Sample coated with sinapinic acid. 13x13 mm^2, 114x114 pixels, pixel size 115x115 μm^2, 150 laser shots per pixel. **C:** Overlay between the two images.

Table 1: Secondary ion yields *Y*, disappearance cross sections σ, ion bombardment efficiencies *E*, relative specific data rate $R_{Bi_1^+}$ and useful lateral resolution δL for Bi_n^{q+} bombardment of cholesterol ($[M-H]^+$; *m/z* 385) in the *corpus callosum* of a rat brain section. The grey lines correspond to doubly charged primary ion clusters.

Primary Ion	Energy (keV)	*Y* ($x10^{-4}$)	σ (10^{-13} cm^2)	*E* (10^8 cm^{-2})	$R_{Bi_1^+}$	δL (nm)
Bi_1^+	25	0.836	2.75	3.04	1.00	1148
Bi_3^+	25	7.06	4.14	17.1	2.86	484
Bi_5^{2+}	50	9.91	3.52	2.81	0.52	377

Table 2: Summary of the experimental conditions for the Figures 6, 7, and 9.

Figure Number	Raster Mode	Primary ions /energy (keV)	Primary Ion Dose Density (ions cm^{-2})	Area (μm^2)	Pixels	Pixel size (μm^2)
6	Fig. 5B	Au_3^+/25 keV	4.10^8	16 000x16 000	256x256	62.5x62.5
7	Fig. 5B	Au_3^+/25 keV	4.10^8	16 000x16 000	256x256	62.5x62.5
9	Fig. 5A	Au_3^+/25 keV	$6.5.10^{10}$	500x500	256x256	1.95x1.95

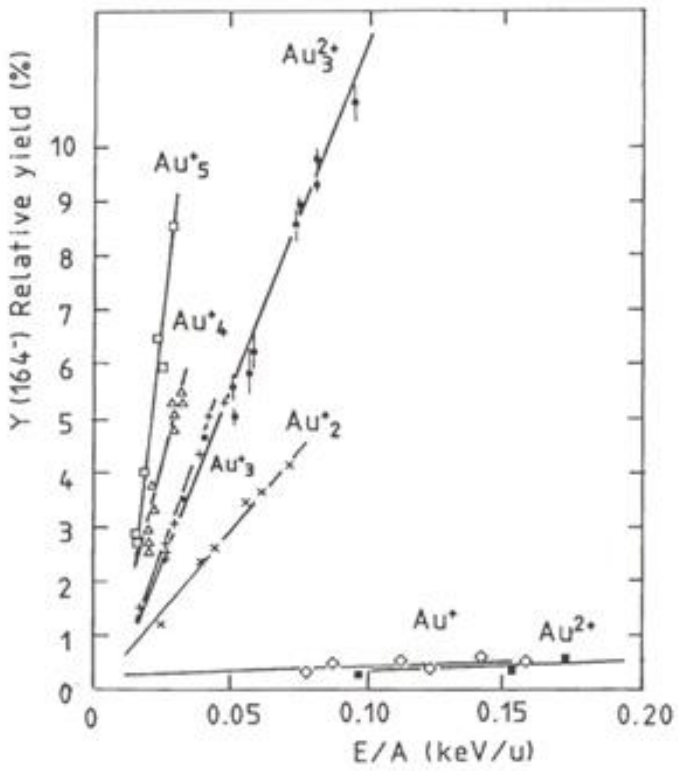
Y (164°) Relative yield (%)
E/A (keV/u)
Au$_3^{2+}$
Au$^+_5$
Au$^+_4$
Au$^+_3$
Au$^+_2$
Au$^+$
Au^{2+}
0
1
2
3
4
5
6
7
8
9
10
0.05
0.10
0.15
0.20

Figure 1

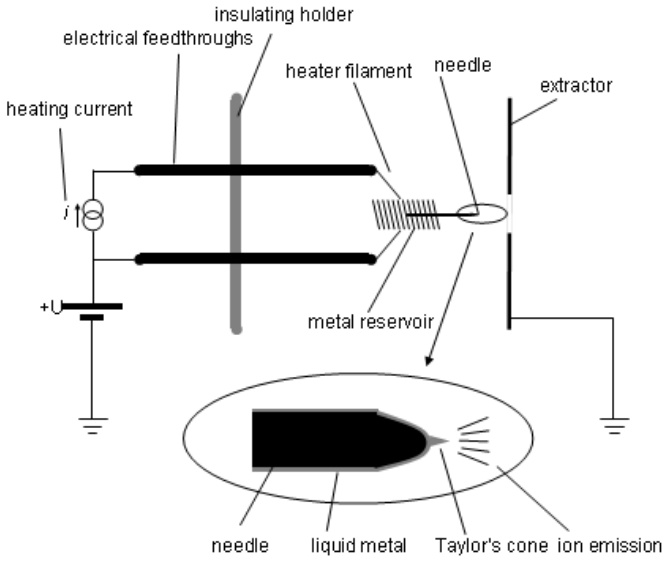
insulating holder
electrical feedthroughs
heater filament
needle
extractor
heating current
+U
metal reservoir
needle
liquid metal
Taylor's cone
ion emission

Figure 2

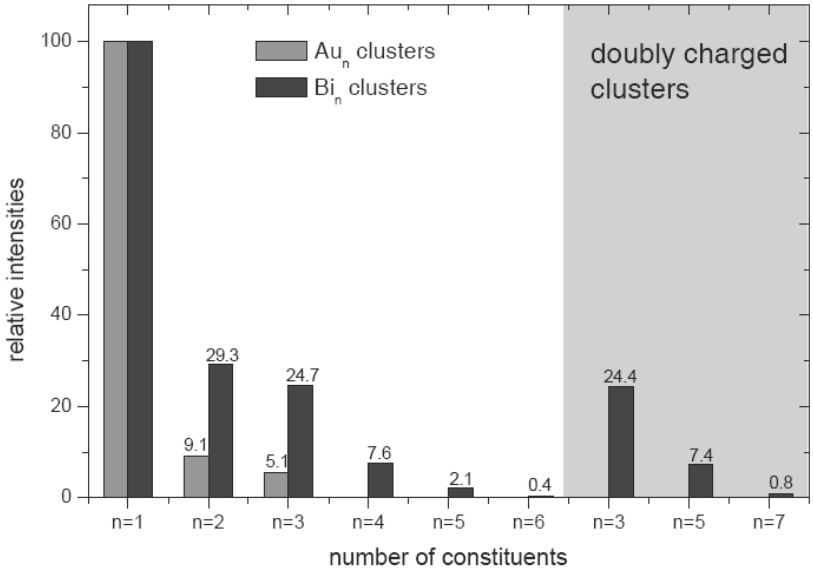
relative intensities
number of constituents
Au$_n$ clusters
Bi$_n$ clusters
doubly charged clusters
100
80
60
40
20
0
9.1
29.3
5.1
24.7
7.6
2.1
0.4
24.4
7.4
0.8
n=1
n=2
n=3
n=4
n=5
n=6
n=3
n=5
n=7

Figure 3

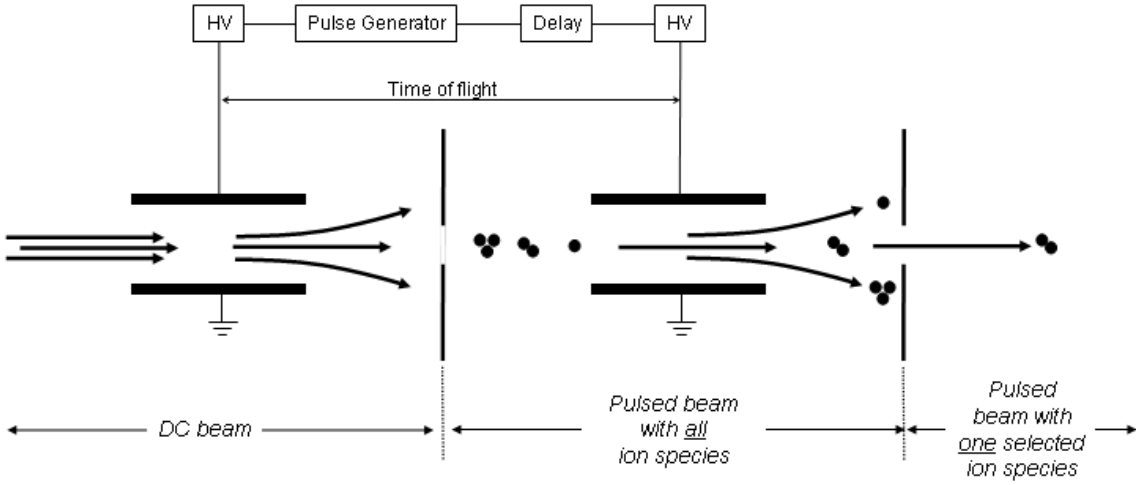
HV
Pulse Generator
Delay
HV
Time of flight
DC beam
Pulsed beam with all ion species
Pulsed beam with one selected ion species

Figure 4

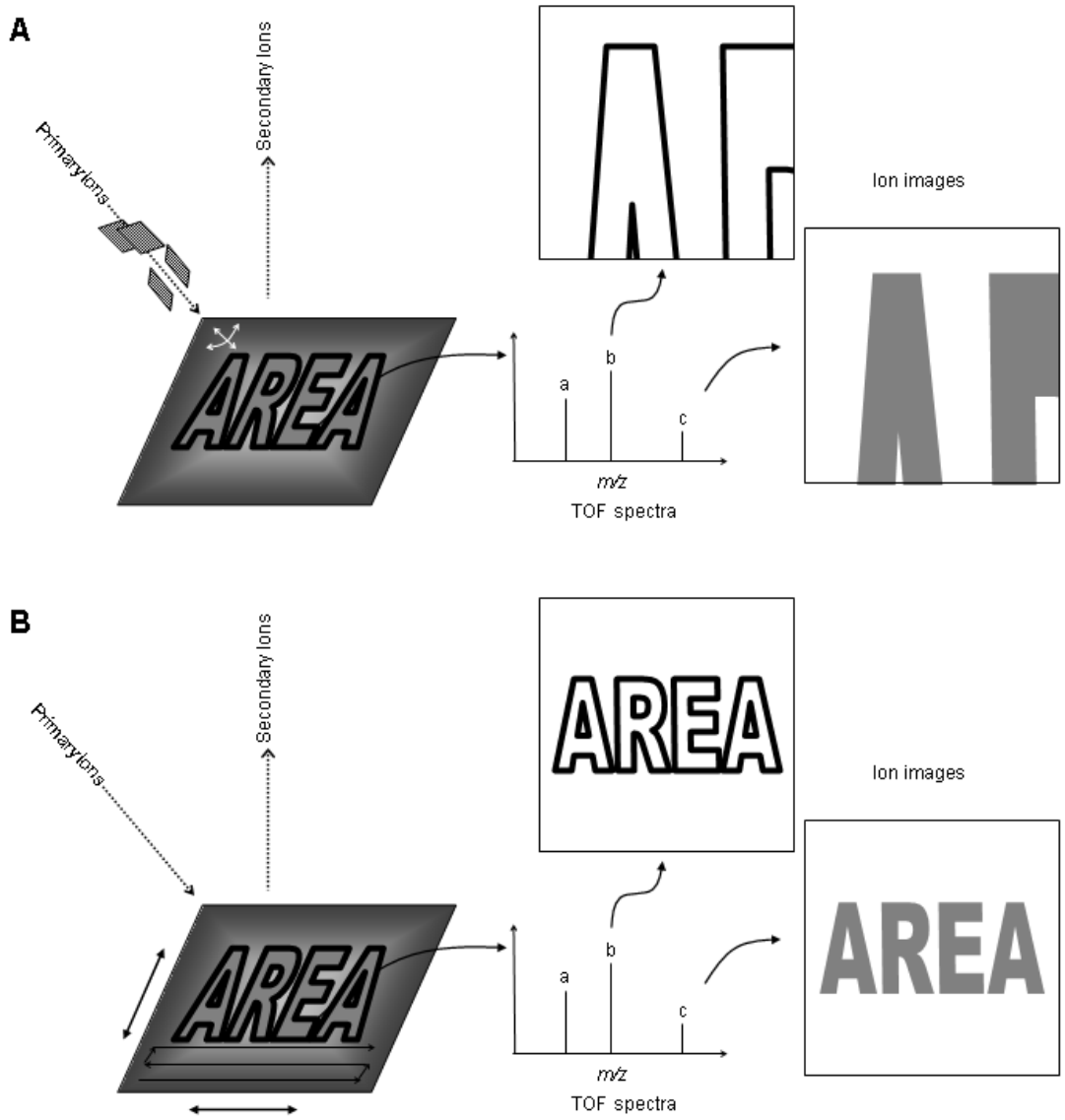
A
Secondary Ions
Primary Ions
AREA
a
b
c
m/z
TOF spectra
Ion images
B
Secondary Ions
Primary Ions
AREA
a
b
c
m/z
TOF spectra
Ion images
AREA

Figure 5

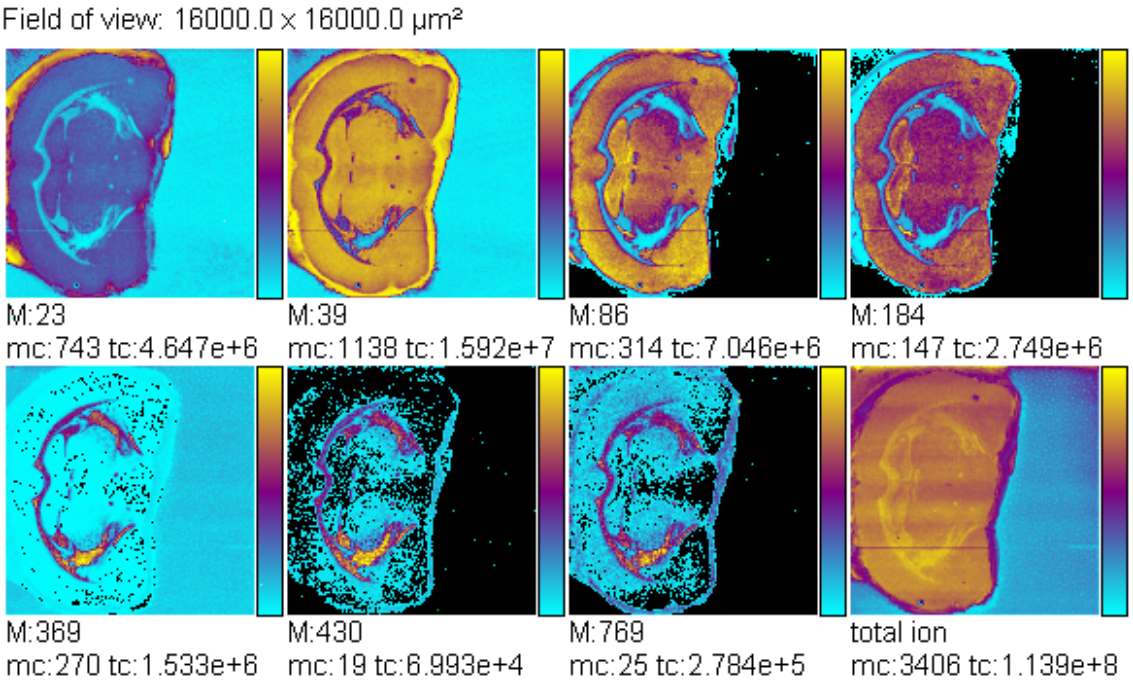
Field of view: 16000.0 x 16000.0 µm²
M:23
mc:743 tc:4.647e+6
M:39
mc:1138 tc:1.592e+7
M:86
mc:314 tc:7.046e+6
M:184
mc:147 tc:2.749e+6
M:369
mc:270 tc:1.533e+6
M:430
mc:19 tc:6.993e+4
M:769
mc:25 tc:2.784e+5
total ion
mc:3406 tc:1.139e+8

Figure 6

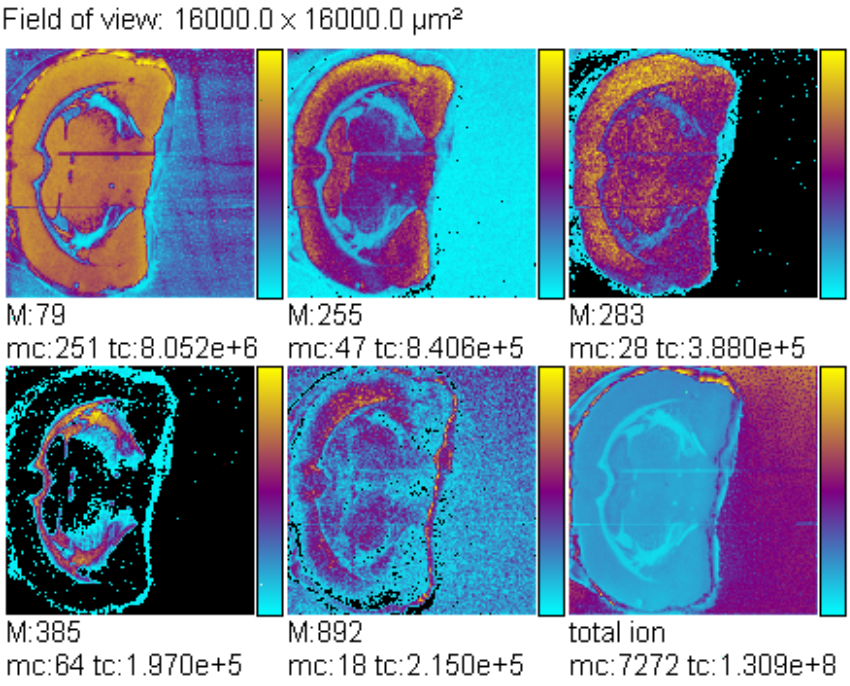
Field of view: 16000.0 x 16000.0 µm²
M:79
mc:251 tc:8.052e+6
M:255
mc:47 tc:8.406e+5
M:283
mc:28 tc:3.880e+5
M:385
mc:64 tc:1.970e+5
M:892
mc:18 tc:2.150e+5
total ion
mc:7272 tc:1.309e+8

Figure 7

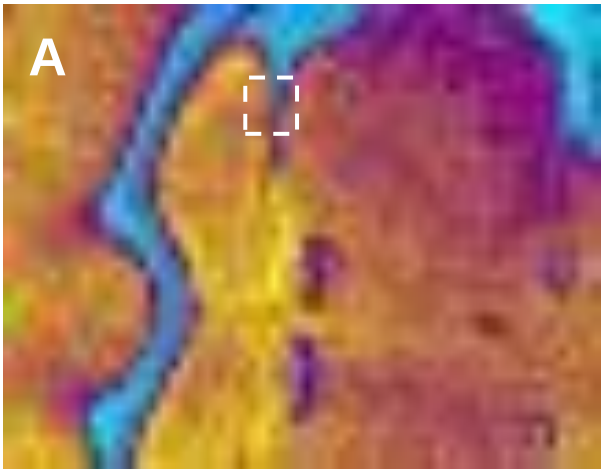

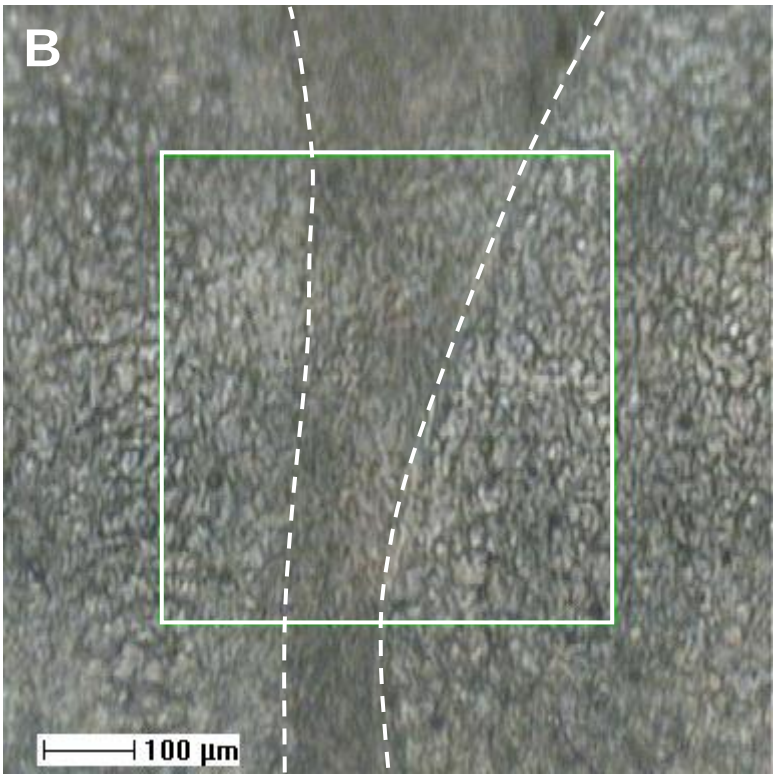

Figure 8

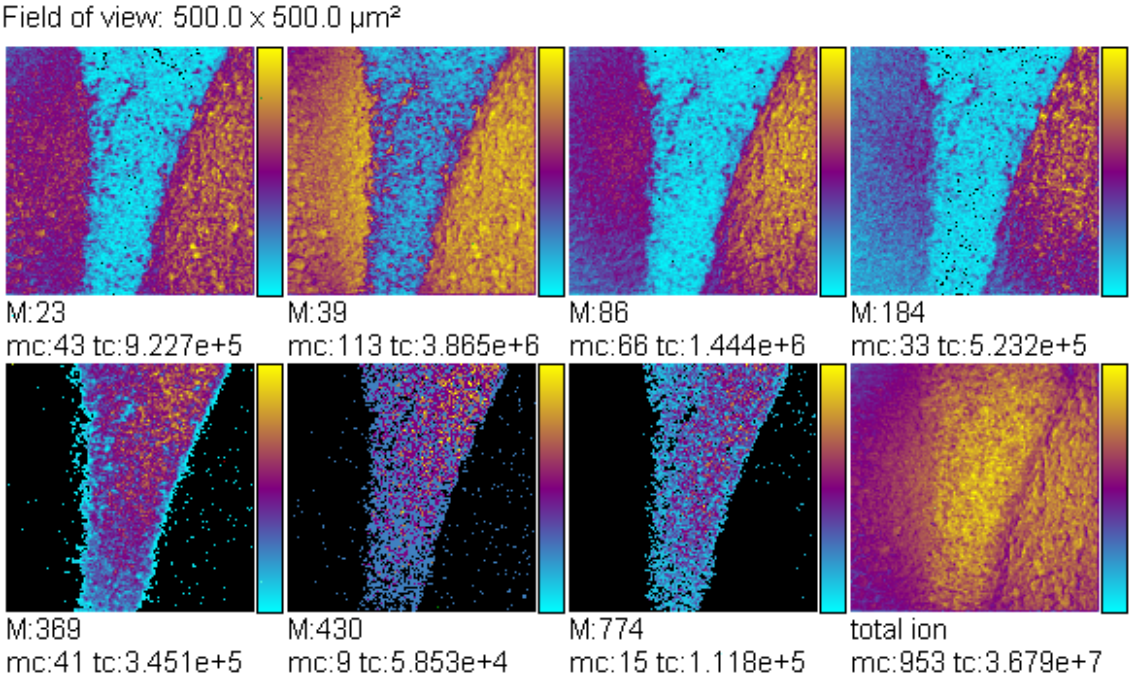
Field of view: 500.0 × 500.0 µm²
M:23
mc:43 tc:9.227e+5
M:39
mc:113 tc:3.865e+6
M:86
mc:66 tc:1.444e+6
M:184
mc:33 tc:5.232e+5
M:369
mc:41 tc:3.451e+5
M:430
mc:9 tc:5.853e+4
M:774
mc:15 tc:1.118e+5
total ion
mc:953 tc:3.679e+7

Figure 9

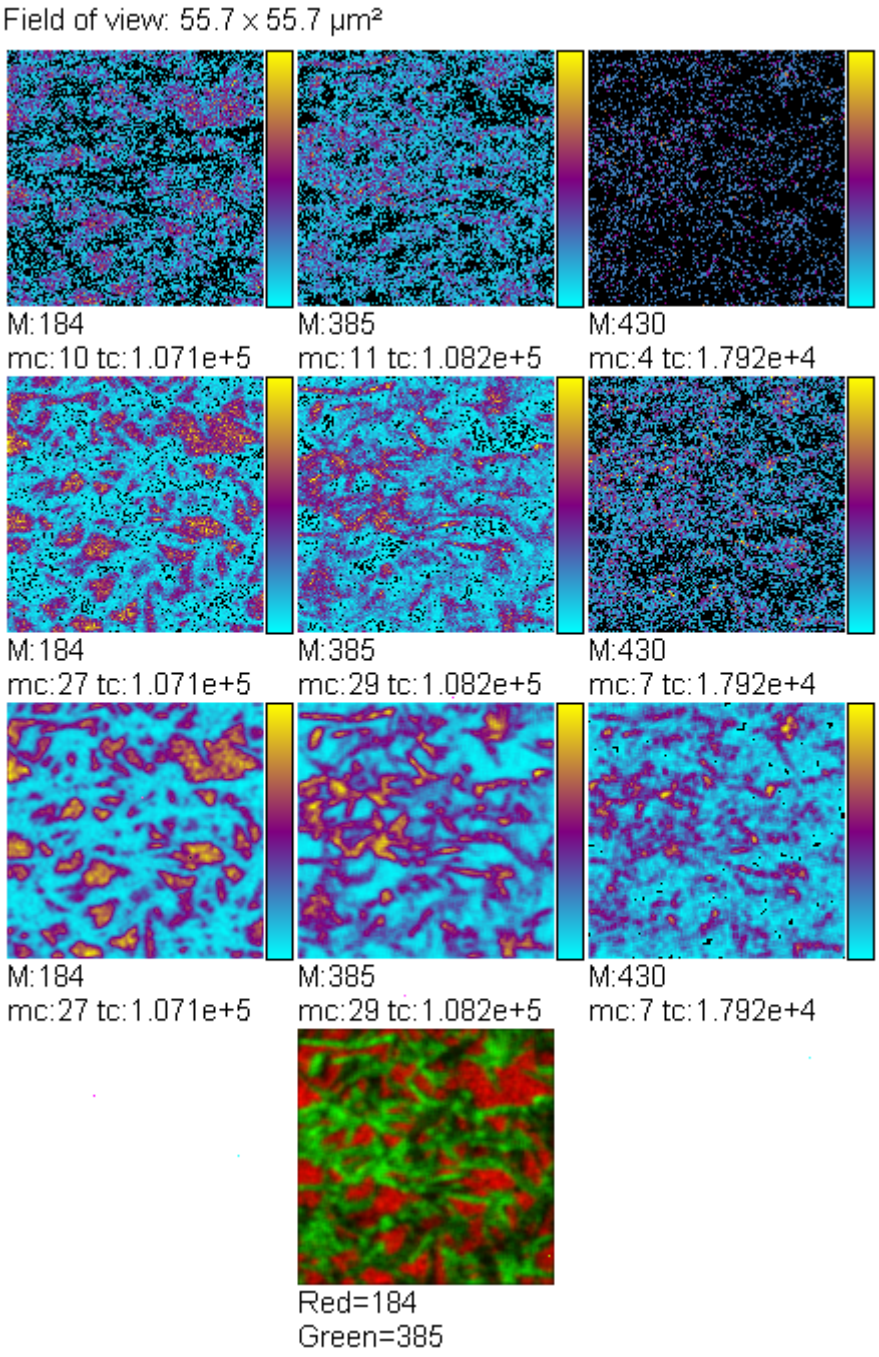
Field of view: 55.7 x 55.7 µm²
M:184
mc:10 tc:1.071e+5
M:385
mc:11 tc:1.082e+5
M:430
mc:4 tc:1.792e+4
M:184
mc:27 tc:1.071e+5
M:385
mc:29 tc:1.082e+5
M:430
mc:7 tc:1.792e+4
M:184
mc:27 tc:1.071e+5
M:385
mc:29 tc:1.082e+5
M:430
mc:7 tc:1.792e+4
Red=184
Green=385

Figure 10

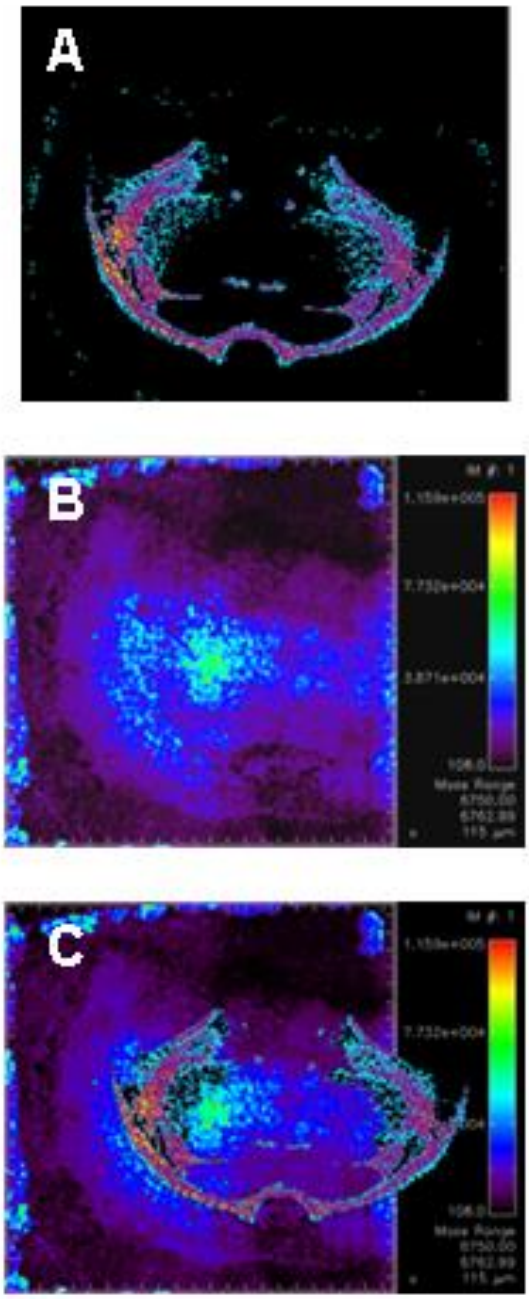

Figure 11